Physics of Fluids ARTICLE scitation.org/journal/phf

Three-dimensional flow structures in X-shaped junctions: Effect of the Reynolds number and crossing angle

Cite as: Phys. Fluids 31, 000000 (2019); doi: 10.1063/1.5087641
Submitted: 3 January 2019 • Accepted: 30 March 2019 •
Published Online: XX XX XXXX

P. G. Correa,[1,a] J. R. Mac Intyre,[1,b] J. M. Gomba,[1,c] M. A. Cachile,[2,d] J. P. Hulin,[3,e] and H. Auradou[3,f]

AFFILIATIONS

[1] Instituto de Física Arroyo Seco—IFAS (UNCPBA) and CIFICEN (UNCPBA-CICPBA-CONICET), Pinto 399, 7000 Tandil, Argentina
[2] Universidad de Buenos-Aires, Facultad de Ingeniería, Grupo de Medios Porosos, Paseo Colón 850, 1063 Buenos Aires, Argentina
[3] Laboratoire FAST, Université Paris Sud, CNRS, Université Paris-Saclay, F-91405 Orsay, France

[a] Fellow of CONICET. **Electronic mail:** pcorrea@exa.unicen.edu.ar.
[b] Fellow of CONICET. **Electronic mail:** jmintyre@exa.unicen.edu.ar.
[c] Researcher of CONICET. **Electronic mail:** jgomba@exa.unicen.edu.ar.
[d] Researcher of CONICET. **Electronic mail:** mcachil@fi.uba.ar.
[e] **Electronic mail:** jean-pierre.hulin@u-psud.fr.
[f] **Electronic mail:** harold.auradou@u-psud.fr.

ABSTRACT

We study numerically the three-dimensional (3*D*) dynamics of two facing flows in an X-shaped junction of two circular channels crossing at an angle α. The distribution of the fluids in the junction and in the outlet channels is determined as a function of α and the Reynolds number *Re*. Our goal is to describe the different flow regimes in the junction and their dependence on α and *Re*. We also explore to which extent two-dimensional (2*D*) simulations are able to describe the flow within a 3*D* geometry. In the 3*D* case, at large *Re*'s ($\gtrsim$50) and α's ($\gtrsim$60°), axial vorticity (i.e., parallel to the outlet axis) of magnitude increasing both with α and *Re* develops in the outlet channels a structure that cannot be reproduced by 2D numerical simulations. At lower angles ($\alpha \lesssim 60°$), instead, a mean vorticity component perpendicular to the junction plane is present: both its magnitude and the number of the corresponding vortices (i.e., recirculation zones) increase as α decreases. These vortices appear in both 2*D* and 3*D* simulations but at different threshold values of α and *Re*. At very low *Re*'s ($\lesssim$5) and α's (~15°), the flow structure in 3*D* simulations is nearly 2*D* but its quantitative characteristics differ from 2*D* simulations. As *Re* increases, this two-dimensionality disappears, while vortices due to flow separation appear in the outlet channels.

I. INTRODUCTION

Many industrial and natural processes such as droplet formation, mixing enhancement, or chemical reactions[1,2] require that two or more fluids be brought into contact. A simple method that does not involve moving elements and can be easily scaled down is the simultaneous injection of the fluids in crossing channels.[3,4] The flow configuration is a crucial parameter, and depending on the applications and processes considered, several geometries can be used, the simplest being X-, Y-, or T-shaped junctions.[5] Previous studies[6,7] have studied the flow at the outlet of a T-shaped junction of channels of rectangular cross section as a function of the Reynolds number *Re* by injecting dye allowing one to visualize the local structure of the flow. Above critical values (Re_c ~ 150), one or several vortices of axis parallel on the mean flow appear and induce a transverse transport which favors the interpenetration of the two fluids and, as a result, mixing.[8] In the present study, we focus instead on flows in X-shaped junctions like the one sketched in Fig. 1. More specifically, we study the influence of both the crossing angle α and the Reynolds number *Re* on the flow structure. The present study provides useful information for applications that require extensional flows and for the mixing of liquid species.

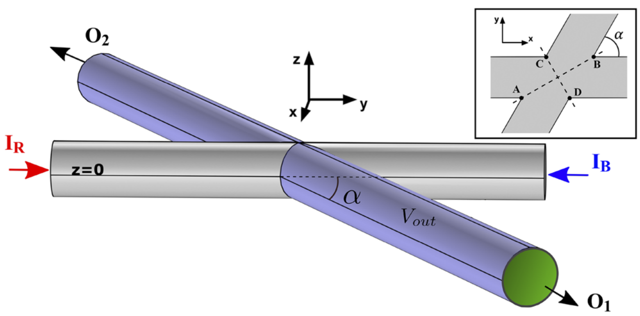

FIG. 1. 3*D* X-shaped junction with two facing inlets (I_R and I_B) and outlets (O_1 and O_2). Here, the indices *R* and *B* correspond, respectively, to the "red" and "blue" fluids referred to below; α: acute crossing angle; V_{out}: volume inside outlet tubes (gray-blue wall) between sections O_2 (in green) and O_1 at a distance of 8.75*d* from the junction center (*d* = tube diameter, $V_{out} = 13.75d^3$). Inset: major (*AB*) and minor (*CD*) axes of symmetry in the crossing region of the junction.

Efficient mixing of two fluids through transverse diffusion across their interface requires that they remain in contact along the largest distance possible to increase the exchange flux between them. In an X-shaped junction, this may be achieved by injecting one of the fluids into one of the channels while the second one flows into the junction from the two channels closest to the inlet one;[9] the two fluids get in contact inside the junction, and the mixture is evacuated through the fourth channel. A second possibility is to inject the two fluids into facing inlets, as depicted in Fig. 1: in this case, mixing takes place inside the junction and along the outlets. An interesting feature compared to the first setup is that it may generate a homogeneous extensional flow with regions of constant strain-rate and a stagnation point. This property is useful in many areas of research, including studies of polymer macromolecules dynamics,[10,11] of viscoelastic fluid rheology,[12,13] and of the influence of controlled deformations on cells, vesicles, or droplets:[4] we selected therefore this multipurpose configuration for the present work.

Lee and co-workers[14] studied the flow structure within two rectangular-section channels, one over the other, in tangential contact and with the separation wall removed in the region of contact. In this case, the inlets are not in the same plane and never in opposite directions. They found that both the angle between the branches of the junctions and the Reynolds number control the streamline distribution. Cachile *et al.*[15] studied instead the flow and the distribution of the fluids in the outlets when all the channels of the X-shaped junction are in the same plane and the two inlets face each other. Except if $\alpha = 90^\circ$, the fluid injected into a given inlet flows dominantly (and, even, completely below a critical angle of $\alpha_c = 33.8^\circ$) out of the nearest outlet (i.e., the channel forming an acute angle α with the inlet). In the same paper, two-dimensional (2*D*) numerical simulations in the limit $Re \ll 1$ relate this partitioning of the fluids between the different outlets to the variations of the structure of the flow. For $\alpha < \alpha_c$, the occurrence of a stagnation point in the junction depends on the angle and it may be replaced by vortices spanning across the junction and of number increasing as α decreases. The appearance of such new structures prevents the exchange of fluids between the two sides of the junction and, therefore, reduces mixing at low α.

In T-shaped mixers, the first axial vortices originate from the stagnation point located on the back-wall and facing the outlet.[6,7] The streamlines coming from facing inlets only cross the symmetry plane of the outlet channel for $Re \geq Re_c \approx 150$. In X-shaped junctions, instead, this same stagnation point is located at the center of the junction where the axes of the different channels intersect. A recent study,[16] performed on an X-shaped junction made of slots of various aspect ratios, showed that for channels of square cross sections, Re_c falls to 40. This is due to the fact that it is easier to start the fluid rotation corresponding to the appearance of a vortex in the middle of the fluid volume (X-shaped junction) than close to a wall (T-shaped junction). As a result, mixing may be expected to be more efficient in X-shaped junctions than in T-shaped ones.

In view of the strong influence of the flow structure and, particularly, of the appearance of vorticity and recirculation structures on mixing in channel junctions, the present work reports numerical simulations of mixing flows of two fluids in X-shaped junctions. The two fluids are injected into two circular tubes [three-dimensional (3*D*) simulations] or into parallel wall channels (2*D* runs), facing each other, and flow out of two other facing channels. Here, we study numerically the distribution of the flows of the two fluids in the outlets and, more specifically, the vorticity components perpendicular to the junction planes and those parallel to the axis of the outlet. In all these simulations, the key control parameters are the Reynolds number of the flow and the angle between the channels. Here, we deal with low and moderate Reynolds numbers up to $Re \leq 80$: this range was chosen because it corresponds to practical applications to fluidic circuits with small channel apertures and/or to many viscous fluids of practical interest. Note that even at the upper limit of this range, flow remains stationary with a velocity field and a distribution of the fluids independent of time.

There are two objectives for the present simulations: a first one is to analyze the dependence on α and *Re* of the occurrence and magnitude, in the outlet channels, of axial vorticity which may significantly influence mixing. The second objective is to determine whether full 3*D* simulations are mandatory in order to describe correctly the flow in the junction or if less computationally expensive 2*D* simulations may give acceptable approximations in some ranges of values of α and *Re*. This has been evaluated by performing also 2*D* simulations in a broad range of α and *Re* values.

Puzzling physical questions arise when dealing with these objectives. Regarding the axial vorticity, the present geometry with circular tube sections and a variable angle α differs from that of Haward *et al.*[16] (rectangular section of variable aspect ratio and constant angle $\alpha = 90^\circ$). It is likely that the loss of symmetry due to the deviation of α from 90° in our simulations will result in a change of the threshold Re_c: if this is the case, will this variation be analogous to that reported by Haward *et al.* keeping $\alpha = 90^\circ$ and varying the aspect ratio of the section. Also, Haward *et al.* characterize quantitatively the development of the axial vorticity from the variation with *Re* of an order parameter derived from the flow field: it will be informative to compute this parameter in our experiment and compare the two variations with *Re* in order to test the similarity between the two phenomena. Regarding the case of lower angles α, the recirculation zones (called vortices in the following) of axis perpendicular to the junction plane mentioned above have been previously studied in the limit of very low Reynolds numbers:[15] how do their number and geometry vary when Re increases and inertial effects become significant?

This paper is organized as follows. Section II presents the geometry and the numerical method used to compute the flow. Section III presents the qualitative features of the flows for three different junction angles α and two different Reynolds numbers Re for two-dimensional ($2D$) and, then, three-dimensional ($3D$) simulations and compares them. Then, we analyze in detail the maps of the flow regimes as a function of α and Re and the variation of the mean vorticity components $\langle \omega_{axial} \rangle$ (axial, i.e., parallel to the outlet axis) and ω_z (transverse, i.e., perpendicular to the junction plane) as a function of these same variables. We then discuss the particular case of junctions of low angles in Sec. V. In Sec. VI, we discuss the dependence of the flow fields and of $\langle \omega_{axial} \rangle$ and $\langle \omega_z \rangle$ on Re and α and on the dimensionality ($2D$ or $3D$). We also evaluate the implications of these results on mixing and the similarity with the instability reported by Haward *et al.*

II. FLOW GEOMETRY AND NUMERICAL PROCEDURE

The X-shaped junction consists of two channels of same circular cross section ($3D$ simulations) or bounded by parallel lines ($2D$ simulations). In both cases, the channels intersect at an acute angle α (Fig. 1). Two identical incompressible fluids (called "red" and 'blue" in the following) are injected into the two corresponding facing inlets. The two fluids flow simultaneously out of each outlet O_1 and O_2 in variable relative proportions depending on α and Re (the relative fractions of the fluids are exchanged between O_1 and O_2 in order to conserve mass). The flow is characterized by following the streamlines from the inlets to the outlets. The diameter d of the channels ($3D$ simulations) and the distance between the parallel channel walls ($2D$ simulations) are both 4×10^{-3} m, and the kinematic viscosity of the fluid is taken equal to $\nu = 10^{-6} \times \mathrm{m}^2\ \mathrm{s}^{-1}$ (close to that of water at 20 °C).

The numerical simulations of the flow within the junctions are performed using the finite element method. The boundary conditions are no-slip at all walls, the Poiseuille flow in both inlets, and zero pressure at the outlets. In both the $2D$ and $3D$ flow simulations, the fluid velocity and the pressure gradients are initially zero. At the origin time, two same Poiseuille flows are applied at the inlets I_R and I_B and one lets the flow velocity field establish itself until a stationary flow regime is reached. Since the inflows at I_R and I_B and the densities and viscosities of the two fluids are assumed to be equal, the characteristics of the flow only depend on the angle α and the Reynolds number $Re = V_m d/\nu$ (choosing Re rather than the mean inlet flow velocity V_m as the control parameter extends the validity of the results to fluids of other viscosities). In our simulations, the Reynolds numbers ranged between 10 and 80 (i.e., $2.5 \times 10^{-3} \le V_m \le 2 \times 10^{-2}$ m s^{-1}). These values are low enough so that no oscillatory flow component appears and a stationary flow regime is reached.

The Navier-Stokes and continuity equations,

$$\rho \frac{\partial \mathbf{u}}{\partial t} + \rho \mathbf{u} \cdot \nabla \mathbf{u} = \rho \mathbf{g} - \nabla p + \mu \nabla^2 \mathbf{u}, \tag{1a}$$

$$\nabla \cdot \mathbf{u} = 0, \tag{1b}$$

are solved for different inflow rates and angles α. Here, $\mathbf{u}$ is the velocity of the flow, p is the pressure, ρ and μ are the density and dynamic viscosity of the fluid, respectively, and $\mathbf{g}$ is the acceleration of gravity. For $3D$ simulations, Eq. (1) is solved through an iterative method, the Generalized Minimal RESiduals (GMRES), preconditioned using a standard multigrid algorithm.[17] This method is preferred to direct methods because it has a good accuracy and requires shorter computing times.[18,19]

In the present simulations, both time-dependent variables, i.e., the velocity field and the pressure, are solved by means of a backward differentiation scheme with adaptive time stepping.[20] The typical initial time step is of order 10^{-5} s when the solution varies rapidly, and at long times, when the solution is near its stationary limit, it is of the order of 10^{-1} s. In order to estimate and control the error at each time step, we use a weighted root-mean-square norm

$$\mathrm{norm}(E) = \left(\frac{1}{N} \sum_i \left(\frac{E_i(X)}{W_i} \right)^2 \right)^{1/2}, \tag{2}$$

where $E_i(X)$ is the estimate by the solver of the error on the variable X corresponding to the degree of freedom i ($1 \le i \le N$) and occurring during a time step. The weights W_i are given by[20]

$$W_i = Rtol\,|x_i| + Atol, \tag{3}$$

where x_i is the corresponding component of the solution vector. The absolute tolerance $Atol$ is set to 5×10^{-4} (with units of the corresponding variable) and $Rtol = 10^{-2}$ (dimensionless). The step is accepted if norm$(E) < 1$.

The junction is discretized with an unstructured mesh using finer elements near the walls, corners, and in the crossing region of the junction, where the velocity gradients are larger. A convergence study is carried out to define reliable mesh parameters that ensure a reasonable balance between accuracy and computing time. Note that the number of mesh elements depends on the angle α due to the increase in the volume of the crossing region for decreasing α. As an example, we use 650 000 mesh cells for $\alpha = 90°$ and 11 200 000 for $\alpha = 15°$.

For testing the numerical method, we consider a junction with $\alpha = 90°$ and an inlet flow corresponding to $Re = 10$. As explained in detail below, a symmetrical extensional flow develops in the junction. The flow varies with time until a steady state solution is reached and symmetrical flow structures are obtained in the center of the junction. At higher Re's, we also check the reliability of the results by comparing them to those obtained with the PARallel DIrect sparse SOlver: PARDISO,[21] an algorithm of high accuracy but computationally too expensive for a parametric study. For the values of the physical control parameters used in the $3D$ simulations, the typical time lapse necessary for reaching the steady state is about 1 s for the smaller angles and 10 s for the larger ones.

For $2D$ simulations, we employed the solver PARDISO since the smaller number of elements makes the computation time acceptable. In this case, after the convergence study, we find that using 15 000 mesh elements for $\alpha = 90°$ and 200 000 elements for $\alpha = 15°$ allows us to get accurate solutions. Here, the transition to the steady state requires less than 2 s.

We quantify inertial effects in the flow by varying the Reynolds number, which is done by changing the inlet flow speed. Additionally, we evaluate the volume average of the vorticity components over a volume V_{out} located between two sections of the outlet tubes which is constant with α (in gray-blue in Fig. 1). The vorticity components of interest are the axial $\langle \omega_{axial} \rangle$ and transverse $\langle \omega_z \rangle$ ones defined below

$$\langle \omega_{axial} \rangle = \frac{1}{V_{out}} \left| \int_{V_{out}} \omega_{axial}\, dV \right|, \tag{4}$$

$$\langle \omega_z \rangle = \frac{1}{V_{out}} \left| \int_{V_{out}} \omega_z\, dV \right|. \tag{5}$$

Defining the volume of integration V_{out} in this way allows us to take into account the contributions to $\langle \omega_{axial} \rangle$ and $\langle \omega_z \rangle$ of both the rotation of the fluid around the axis of the outlets and the vortices produced in the crossing region of the junction, respectively. In 2*D* simulations, the volume V_{out} is replaced by a band of same length as V_{out}, of width equal to the diameter *d* of the tubes in the 3*D* simulations, and of area $17.5d^2$.

III. QUALITATIVE CHARACTERISTICS OF THE DIFFERENT FLOW REGIMES

In this section, we describe and compare the structures of the flow fields obtained from simulations in 2*D* and 3*D* geometries. The study is particularly focused on the dependence on both *Re* and *α* of the structure of the streamlines at the center of the junction. We map then the flow regimes observed in both cases as a function of *Re* and *α*.

A. Flow fields from 2D simulations

Figure 2 shows the flow patterns in 2*D* X-shaped junctions for three crossing angles. For $\alpha = 20^\circ$ and 40°, each inlet flow reaches the intersection of the junction and bounces back downstream toward the outlet branch located at an angle *α* from the corresponding inlet direction. For $\alpha = 65^\circ$, a minor fraction of the inlet flow moves into the other outlet. A key characteristic of these flows is the development of vortices marked by "closed" streamlines in the junction region. Varying *α* and/or *Re* may modify the size and number of the vortices through successive divisions or merging.

The number of vortices observed for $Re = 10$ decreases from two for $\alpha = 20^\circ$ [Fig. 2(a)] to one for $\alpha = 40^\circ$ [Fig. 2(c)] and zero for $\alpha = 65^\circ$ [Fig. 2(f)]. These vortices are either aligned with the major axis of symmetry (segment *AB* in Fig. 1) or located at its center.

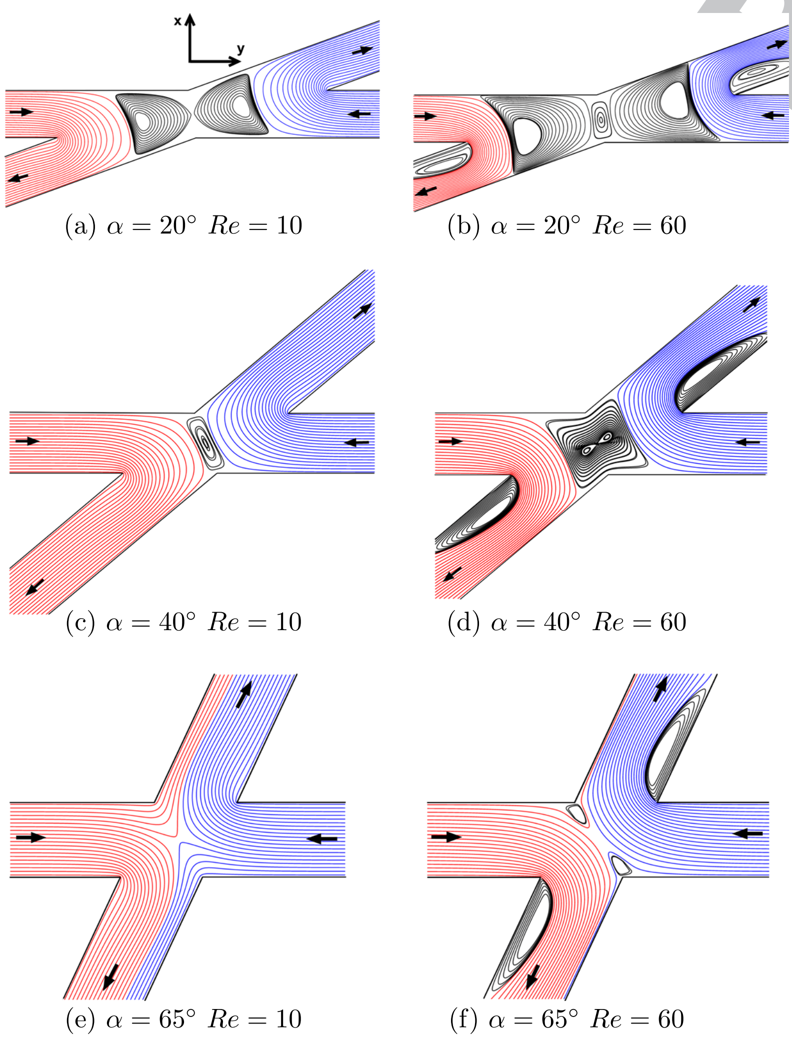

FIG. 2. Streamlines in 2*D* junctions of different angles ($\alpha = 20^\circ$, 40°, and 65°) at two Reynolds numbers (Re = 10 and 60). Blue and red streamlines originate from each respective inlet. Black streamlines mark the vortices.

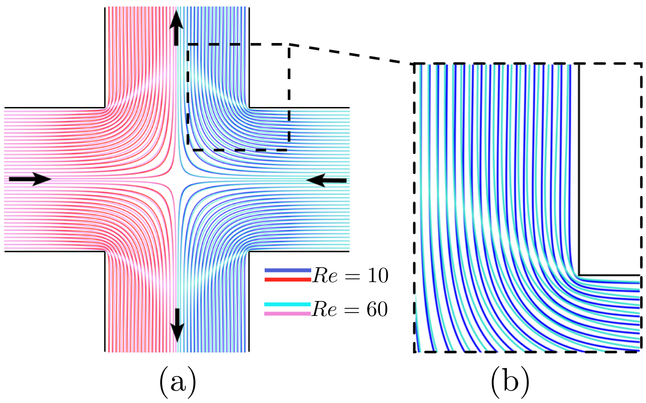

FIG. 3. (a) Overlap of streamlines corresponding to Re = 10 (dark blue) and 60 (light blue) in a 2D junction with α = 90°. Streamlines originate from each inlet. (b) Close-up view of the region bounded by a dashed rectangle in (a).

For Re = 60, this same number decreases from three for α = 20° [Fig. 2(b)] to one (containing two smaller vortices) for α = 40° [Fig. 2(d)] and zero for α = 20° [Fig. 2(f)]: however, in this latter case, there are two small vortices with their centers aligned, this time, with the perpendicular segment CD and located near the tip of the junctions of angle $\pi - \alpha$.

An important additional feature of the flow, for the highest Re value investigated, is the growth of vortices attached to a wall in both outlet channels [Figs. 2(b), 2(d), and 2(f)]: these vortices have a different origin and are due to flow separation at the tip of the junctions of angle α between the inlet and outlet channel walls. Also, when α decreases, the streamlines become tightly packed in their region of high curvature near these tips, implying an increased local velocity.

For α = 90°, instead, no recirculation flow is observed in the whole range of Re values investigated, whether in the center part of the junction or in the outlet channels. As the inflow of each fluid reaches the junction, it splits into two equal flows moving

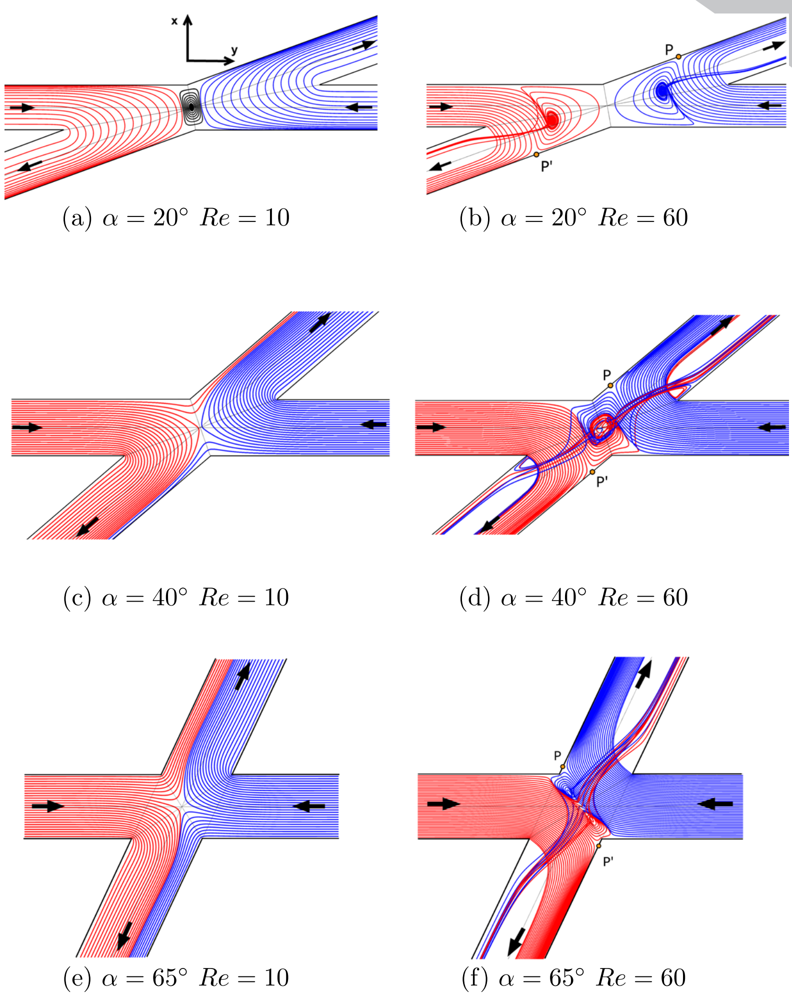

FIG. 4. Streamlines in 3D junctions for different angles α and two different Reynolds numbers Re = 10 and 60. Blue and red streamlines originate in the middle plane of each inlet. Black streamlines correspond to closed trajectories. White spaces in the outlet channels correspond to streamlines originating at the inlets but with $z \neq 0$ (not shown for clarity). P, P′: stagnation points on the walls.

downstream in opposite directions. Moreover, the flow fields observed for Re = 10 and Re = 60 are almost the same [Fig. 3(a)]; the difference is the largest downstream of the corners of the junction [Fig. 3(b)].

B. Flow fields from 3D simulations

Figure 4 displays streamlines obtained from 3D simulations performed for the same α's and Re's as in the 2D geometries in order to determine the similitudes and differences. For α = 20° and Re = 10 [Fig. 4(a)], the inlet flows are similar to those observed in the 2D case [Fig. 2(a)] but they are separated by only one vortex at the center of the junction instead of two for 2D. Still for Re = 10, recirculation disappears for both α = 40° [Fig. 4(c)] and α = 65° [Fig. 4(e)]. In the first case, recirculation was present in the corresponding 2D simulation [Fig. 2(c)]: this confirms the reduction of the number of vortices in the 3D geometry already noted for α = 20°. For both α = 40° and 65°, the incoming streamlines split into two sub-streams of different strengths with the appearance of a stagnation point at the center of the junction. The major sub-stream follows the higher curvature path, and the smaller one flows into the other outlet channel with a lower curvature path. The fraction of the streamlines with the smaller curvature increases with α [Figs. 4(c) and 4(e)] like in 2D geometries.[15] For Re = 10, at all angles, no clear tridimensional feature is visible on the streamlines unlike, as will be seen now, for higher Reynolds numbers.

When Re increases to Re = 60, two vortices appear for α = 20° (one more than for Re = 10) and occupy most of the junction [Fig. 4(b)]. Unlike in Figs. 4(a) and 2(b), here, the vortical streamlines have "open" trajectories with clear 3D structures, as shown in Fig. 5(a). These start at the inlets, impact the lateral wall close to the stagnation points P and P', pass through the vortex, and join back the main flow in the outlets. The stagnation points P and P' separate these streamlines from those which originate in the same inlet but bounce back directly into the nearest outlet.

Still for Re = 60, but for α = 40° [Figs. 4(d) and 5(b)] and 65° [Figs. 4(f) and 5(c)], the flow displays one or two vortices of open three-dimensional streamlines in the junction center region (instead of none for Re = 10). The higher velocity of the entering flow favors the division into two sub-streams following the flow impingement at the stagnation points P and P' on the lateral wall of outlet branch. For α = 40°, the vortex structure at the center of the junction is generated by the mixing of the two smaller sub-streams (blue and red streamlines). Also, comparing Figs. 4(c) and 4(d) shows that due to the increased influence of inertia, the minor flow component which crosses the center of the junction moves from one side of the outlet channel for Re = 10 to the other for Re = 60. For α = 65°, there are two small vortices of centers aligned along the minor symmetry axis like in the 2D case [Fig. 2(f)]. At both angles, these two sub-streams finally escape the vortex in opposite directions toward the outlet branches.

An interesting feature of the stagnation points P and P' observed for Re = 60 [Figs. 4(b), 4(d), and 4(f)] is that they move toward the center of the junction as α increases. The vortices do the same, and while for α = 20°, they are located along the major symmetry axis of the junction [Fig. 4(b)], and they are almost aligned with the minor axis for α = 65° [Fig. 4(f)]. Finally, like in the 2D geometry, there is a region of flow separation and formation of small vortices downstream of the corner of angle α at the intersection of the inlet and outlet tubes (streamlines are not shown in the graph for clarity, and this region is left empty). We remark that for all flows discussed up to now, the vortex axes are perpendicular to the junction plane (z-direction).

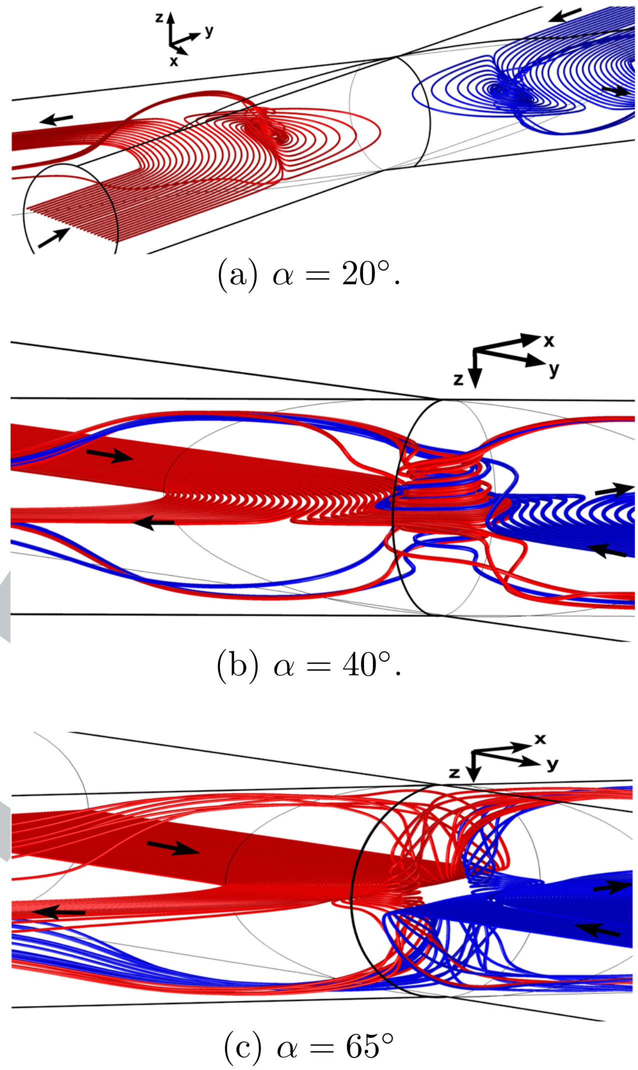

FIG. 5. Perspective view of streamlines corresponding to Re = 60 in 3D junctions with different angles α. All streamlines start at the inlet with a coordinate z = 0.

While for α = 90° and Re = 10, the flow pattern is similar [Fig. 6(a)] to that in the corresponding 2D case (Fig. 3); for Re = 60, it is very different [Fig. 6(b)]. Both inflows cross the plane y = 0 in the center part of the junction, penetrating one from above and the other from below, and develop a swirling motion. Downstream, streamlines are curved and some of them move sideways inside the outlet branches. As a result, an axial vortex appears in this junction and increases the area of the interface between the two liquids, leading to a more efficient mixing. Unlike all flows discussed above for other α values, the axis of the vortex is parallel to that of the outlet

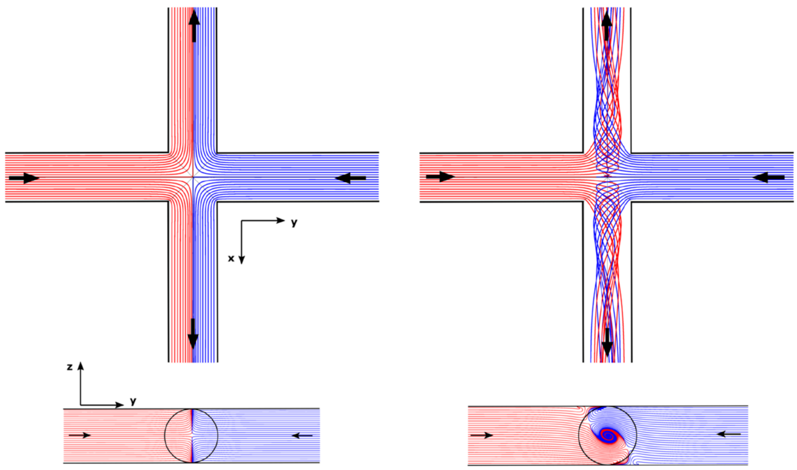

(a) $\alpha = 90^\circ$ $Re = 10$. (b) $\alpha = 90^\circ$ $Re = 60$.

FIG. 6. Streamlines in 3*D* junctions for α = 90° and two different Reynolds numbers. In the top (side) view graphics, the streamlines originate in the inlets in the plane z = 0 (x = 0).

tube and not perpendicular to the plane of the junction as was always the case in the examples of Fig. 4.

Overall, the flow velocity maps obtained in the present section agree qualitatively with the distributions of the flow between the two outlets reported previously[15] for X-shaped junctions of channels with square cross sections. These authors had also noted experimentally the appearance of 3*D* structures of the flow field for $Re \gtrsim 50$. For $\alpha = 90^\circ$, the present results at such Reynolds numbers are qualitatively similar to those obtained by other authors[16] for rectangular channels and will be compared to them in Sec. VI. Regarding this latter work, we performed one validation test in the same geometry as these authors for $Re = 60$ which displayed an excellent agreement with both their numerical and experimental results.

C. Flow regime maps

In this section, we present maps of 2*D* and 3*D* flow regimes in the range of values investigated: $15^\circ \leq \alpha \leq 90^\circ$ and $1 \leq Re \leq 80$. Figure 7 displays a map of the different types of flow structures observed as a function of Re and α in 2*D* numerical simulations. This map complements the information displayed in Fig. 2 and allows us to identify six regimes corresponding to different numbers (and types) of vortices in the junction. For instance, for $Re = 60$, the number of vortices aligned with the major axis AB of the junction (the inset of Fig. 1) or located at its center decreases from four for $\alpha = 15^\circ$ to zero for $\alpha \geq 67^\circ$. The flow field displayed in Fig. 2(f) for $Re = 60$ and $\alpha = 65^\circ$ corresponds to the transition regime between one and zero vortices: one observes then two small vortices but, this time, aligned along the minor axis CD; these may be considered as resulting from the split and size reduction of a single, larger, original vortex. Still for $Re = 60$ but for $\alpha = 40^\circ$, one is near the transition between one and two vortices. One has a single large vortex at the center of the junction, but it contains two smaller vortices aligned along axis AB [Fig. 2(d)]. When the Reynolds number decreases, the number of vortices still deceases when α increases but the values of α corresponding to a given transition are smaller. For instance, for $Re = 10$, the transition between one and zero vortices takes place around $\alpha = 40^\circ$ (instead of around 65° for $Re = 60$). Like in this latter case, one observes also for $Re = 10$ and $\alpha = 40^\circ$ two vortices aligned along the minor axis AB [Fig. 2(c)]. The same trend in the transition angles is observed at lower angles, and, for instance, for $\alpha = 15^\circ$, there are only three vortices at $Re = 10$ instead of four at $Re = 60$.

Figure 8 displays the same map but constructed from 3*D* simulations. The limits of the flow regimes do not coincide with those obtained for the 2*D* case, but the general trend looks similar. The most important difference from the 2*D* map is the appearance at

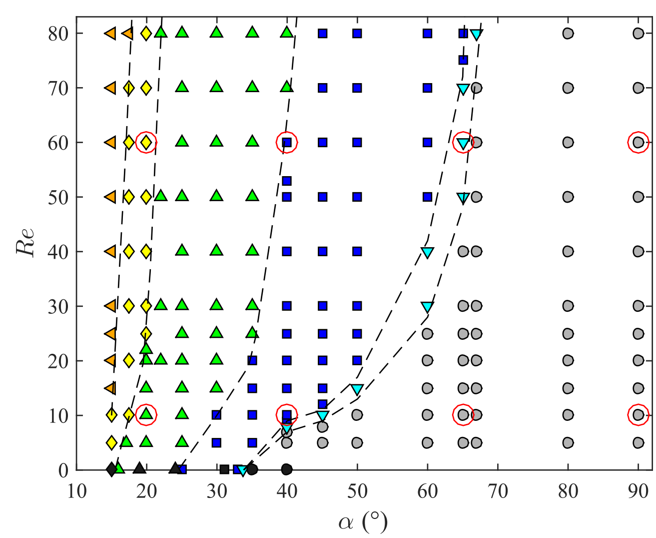

FIG. 7. 2*D* simulations. Map of the different flow configurations observed as a function of α vs Re. Symbols indicate the number of the vortices: gray filled circles, no vortex; navy blue filled squares, one vortex; green filled upward triangles, two vortices aligned along the major axis; blue filled downward triangles, two vortices aligned along the minor axis; yellow filled diamonds, three vortices; and orange filled left pointing triangles, four vortices. Red empty circles: cases presented in Figs. 2 and 3. Black symbols: results of Cachile *et al.* in the limit $Re \to 0$.

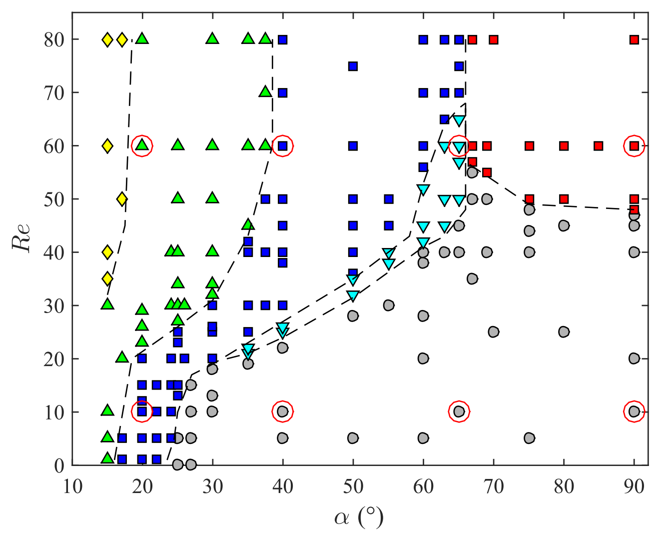

FIG. 8. 3*D* simulations. Map of the different flow configurations as a function of α vs *Re*. Symbols indicate the number and orientation of the vortices observed. Red filled squares: one vortex parallel to the axis of the outlet channels. Other symbols: vortices parallel to the *z* axis. Gray filled circles, no vortex; navy blue filled squares, one vortex; green filled upward triangles, two vortices; blue filled downward triangles, two vortices aligned along the minor axis; yellow filled diamonds, three vortices. Red empty circles: cases presented in Figs. 4–6.

high α's and *Re*'s of a region where the axis of the vortices is not parallel to the z-direction but to the axis of the outlet channels (red symbols in Fig. 8). The maximum number of vortices is three in this diagram while for 2*D* up to four vortices were observed.

IV. AXIAL AND TRANSVERSE VORTICITY COMPONENTS

One of the most striking features of the previous results, with strong relevance to mixing processes, is the transition from vortices of axis perpendicular to the junction plane (observed for most values of the angle α) to vortices of axis parallel to that of the outlet channels (observed for high α and *Re* values, typically $Re \gtrsim 50$ and $\alpha \gtrsim 65°$).

In order to analyze quantitatively this transition as well as the structure of the flow at low angles, we studied the variation of the volume averaged z-vorticity component $\langle \omega_z \rangle$ and of the volume averaged axial vorticity $\langle \omega_{axial} \rangle$ with α and *Re*. Note that by symmetry, the global contributions of the Poiseuille components of the flow at both outlets cancel. Thus, $\langle \omega_z \rangle$ characterizes the nonsymmetrical contributions to the vorticity [Eq. (5)]. In the case of $\langle \omega_z \rangle$, we have also compared the variations obtained from 2*D* and 3*D* simulations ($\langle \omega_{axial} \rangle$ is, of course, zero in the 2*D* case).

Figure 9(a) displays the variations of $\langle \omega_{axial} \rangle$ (3*D*) as a function of *Re* for different angles. For $\alpha = 90°$, $\langle \omega_{axial} \rangle$ increases "suddenly" at $Re \sim 50$ from 0.02 s^{-1} to 0.15 s^{-1} and, then, continues increasing linearly with *Re*. This increment corresponds to the appearance of an axial vortex at $Re_c \simeq 48$, as shown in Fig. 8. For smaller α's, the trend is similar, but Re_c increases as α decreases and the variation close to Re_c is smoother. One notices that for $\alpha = 40°$, $\langle \omega_{axial} \rangle$ is negligible over the whole range of *Re* values explored. When $\langle \omega_{axial} \rangle$ is nonzero, its value for a given *Re* increases with α. Finally, the axial vorticity due to the swirling motion decreases with the down-flow distance due to viscous damping so that most of the contribution to the average comes from the vicinity of the crossing region.

Figures 9(b) and 9(c) display the variation of the transverse vorticity $\langle \omega_z \rangle$ with *Re* for 3*D* and 2*D* simulations, respectively

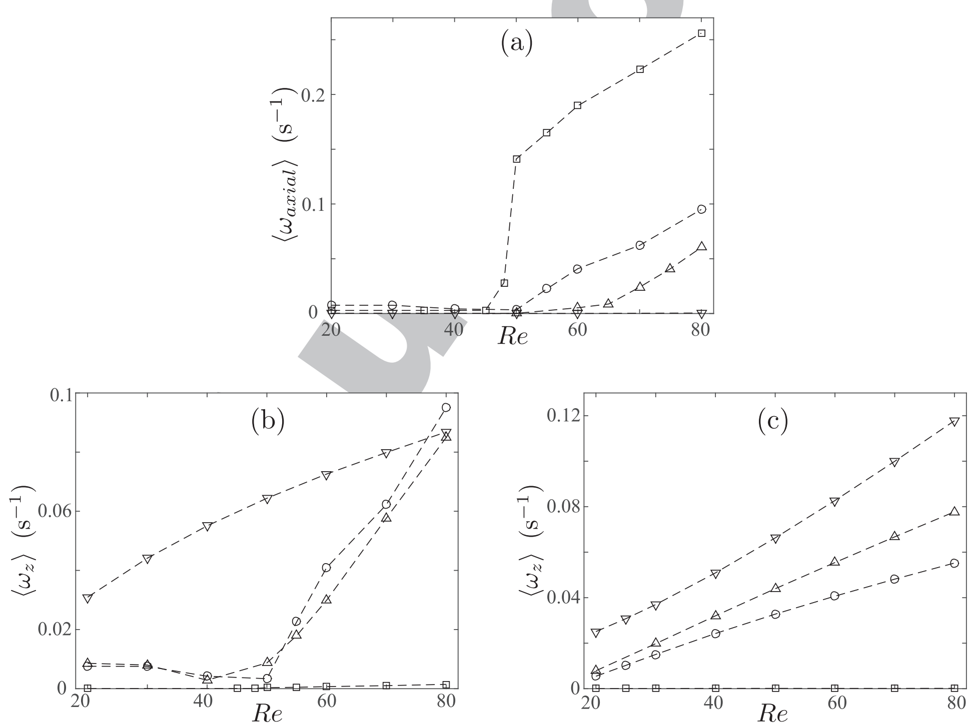

FIG. 9. Variations of the averages $\langle \omega_{axial} \rangle$ and $\langle \omega_z \rangle$ of the axial [(a) 3*D* simulations] and transverse [(b) 3*D*] and [(c) 2*D*] vorticities as a function of *Re* for different angles: $\alpha = 90°$ (empty squares), $\alpha = 69°$ (empty circles), $\alpha = 65°$ (empty upward triangles), and $\alpha = 40°$ (empty downward triangles). The vorticities are averaged over the volume V_{out} defined in Fig. 1.

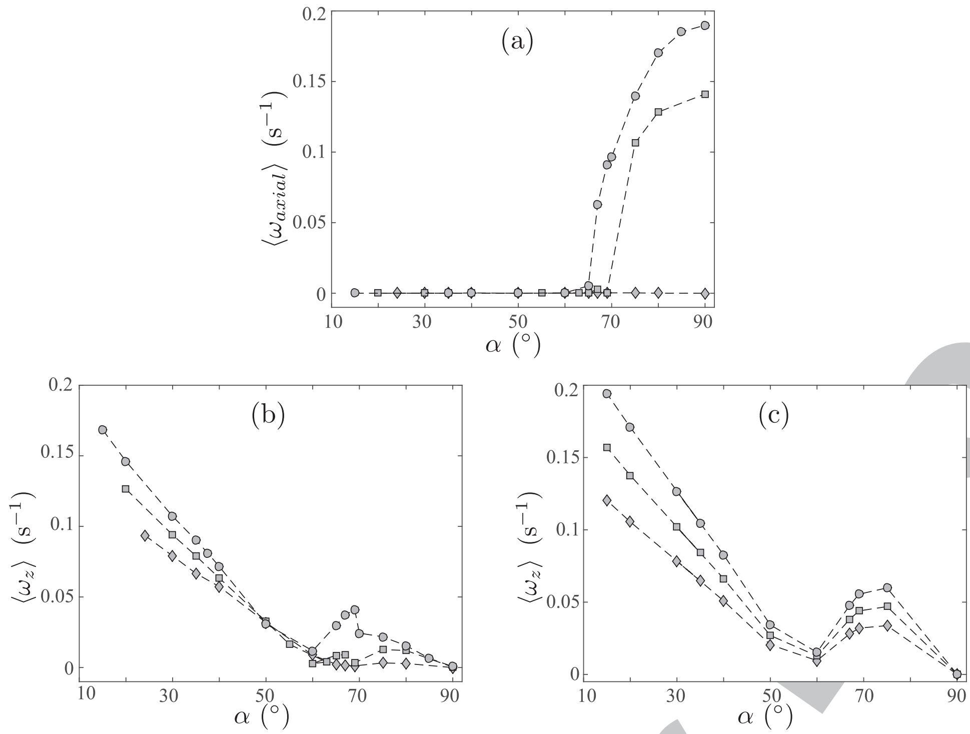

FIG. 10. Variations of the averages $\langle \omega_{axial} \rangle$ and $\langle \omega_z \rangle$ of the axial [(a) 3*D* simulations] and transverse [(b) 3*D*] and [(c) 2*D*] vorticities as a function of α for different Reynolds numbers: $Re = 60$ (gray filled circles), $Re = 50$ (gray filled squares), and $Re = 40$ (gray filled diamonds). The vorticities are averaged over the volume V_{out} defined in Fig. 1.

[the values of α are the same as in (a)]. Like $\langle \omega_{axial} \rangle$, $\langle \omega_z \rangle$ increases globally with *Re* at a given angle but in a different way: while in the 2*D* cases, $\langle \omega_z \rangle$ increases smoothly with *Re*, this is only the case in 3*D* at low angles for which $\langle \omega_{axial} \rangle = 0$ such as $\alpha = 40°$. At higher angles (65° and 69°), instead, $\langle \omega_z \rangle$ remains small and decreases slightly with *Re* before increasing much faster above $Re \sim 50$ in the domain where $\langle \omega_{axial} \rangle$ also starts to increase For $\alpha = 90°$, $\langle \omega_z \rangle$ is nearly equal to zero in all cases (particularly in the 2*D* case) due to the symmetry of the flow. These results indicate a strong relation between the variations of the axial and transverse vorticities.

In Fig. 10(a), the axial component $\langle \omega_{axial} \rangle$ is plotted as a function of α. For $Re = 60$, $\langle \omega_{axial} \rangle$ is negligible up to $\alpha = 65°$, increases abruptly for $\alpha = 69°$, and, then, progressively up to 0.19 s^{-1} at $\alpha = 90°$: this increase marks the development of the swirling motion in the outlets. The variation is similar for $Re = 50$, but the increase takes place at a higher angle (~70°) and with a lower upper limit ≃0.14 s^{-1}. For $Re = 40$, $\langle \omega_{axial} \rangle$ remains always zero, in agreement with Fig. 9(a).

On the other hand, in Fig. 10(b), $\langle \omega_z \rangle$ is observed to decrease steadily for $Re = 60$ from 0.17 s^{-1} to 0.01 s^{-1} as α increases from 15° to 60°. The variation is similar with slightly lower values for $Re = 40$ and 50 and, also, in the 2*D* simulations [Fig. 10(c)]. This is due, in part, to the reduction of both the number of vortices (of axis parallel to *z*) and of the size of the associated vortical regions. However, the dominant contribution to this decreasing trend is the reduced curvature of the streamlines which are less excluded from the region of the vortices. For higher α's, $\langle \omega_z \rangle$ increases slightly between $\alpha = 60°$ and 70°–80° [Figs. 10(b) and 10(c)] due to the appearance of the two small vortices aligned along the minor axis [Fig. 4(f)]. Finally, $\langle \omega_z \rangle$ decreases continuously to zero between $\alpha = 70°$ and 90° due to the reduction of the curvature of the streamlines joining the inlets and the outlets with no vortices present.

Overall, while both the axial and transverse vorticities increase globally with the Reynolds number (with a threshold effect in the vicinity of $Re = 50$), the axial vorticity is only nonzero above a threshold angle and increases at higher angles as a swirling motion appears in the outlet. Instead, at lower α values, the transverse vorticity decreases as α increases: for large enough Reynolds numbers, one has then a transition from transverse to axial vorticity as α increases.

V. FLOW STRUCTURE AT LOW JUNCTION ANGLES

Here, we investigate 3*D* flow at low angles: this is a particularly interesting case because the flow structure is more similar to the 2*D* one, particularly at low Reynolds numbers.

Figure 11 displays the streamlines corresponding to $\alpha = 15°$ at $Re = 5$ and $Re = 60$. Streamlines are plotted at three different heights to depict the internal flow structure. At a low $Re = 5$, the 3*D* streamline pattern closely resembles that observed in the 2*D* case and the flow field has an essentially 2*D* configuration at each height [Fig. 11(c)]. Two vortices with closed streamlines separate the two fluids, as can be seen in Fig. 11(a). The 3*D* effect is only shown in Fig. 11(e) by the small curvature in the y-z plane of the upper and lower sets of streamlines. The recirculation is localized in the center zone of the junction and occupies a small part of the volume of the intersection region. For the same values of α and *Re*, we observed in the 2*D* simulations the formation of three vortices instead of two here (see Fig. 7).

At $Re = 60$, the flow structure is much more three-dimensional even though, in the intersection zone, fluid particles move

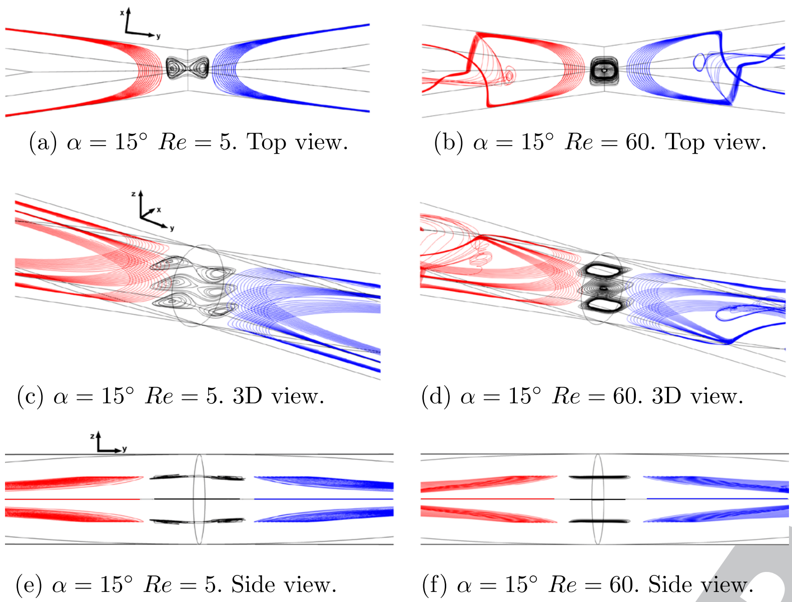

FIG. 11. Top, side, and perspective views of the streamlines in 3*D* simulations for Re = 5 and Re = 60 and for α = 15°. Blue and red streamlines originate from each inlet. Black streamlines are located in vortices.

essentially in planes parallel to (x, y). The flow displays only one vortex in the center of the junction and two vortical structures on each side [Fig. 11(b)]. The central vortex retains a 2*D* configuration of closed streamline layers [see Fig. 11(f)], while the two side vortices present open streamlines and occupy a large part of the junction. These vortical structures are formed of entering streamlines that move toward the center of the junction after impacting the lateral wall in the outlet branch. These streamlines eventually leave the vortex and join the main flow near the outlet. A 3*D* flow pattern is observed in these two vortices in the region close to the mean flow, where the z-coordinate of the streamlines varies [Fig. 11(d)].

VI. DISCUSSION AND CONCLUSION

The present numerical study has characterized extensively the variations of the velocity and vorticity fields in X-shaped junctions with their angle α and the Reynolds number Re. A first important result is that axial vortical structures [Fig. 6(b)] of axis parallel to that of the outlet tubes, in addition to being only present in 3*D* simulations, appear only at large values of α and Re. A major characteristic of these structures is that they may strongly enhance the efficiency of mixing in the junctions as will be shown now.

Figure 12 displays the distribution of the two fluids in an outlet section (in green in Fig. 1) for several values of α and Re = 10 or 60 (thumbnail pictures). The red and blue domains in the figures correspond to zones where the section is intersected by flow-lines corresponding to either the "red" or the 'blue" fluid. For Re = 10, at low angles α, a dominant fraction of the outlet area is occupied by one of the fluids while the two fractions are of the same order at large angles. In both cases, the geometry of the boundary is a smooth, low curvature line: mixing of the two fluids would require, even for α = 90°, molecular diffusion over a distance of the order of the tube radius or more. At Re = 60, at low angles, the geometry of the interface is more complex but there is still a very dominant fraction of one of the fluids and mixing requires molecular diffusion along a large distance and remains inefficient. At large angles, instead, the interface takes a spiral like geometry favoring mixing: it is produced by the axial vorticity which has a large value in these two cases as shown in Fig. 10.

A simple quantitative characterization of these effects is provided by the variation with α and Re of the dimensionless length l_c/d of the boundary between the regions occupied by the two fluids (blue and red on the thumbnail pictures). For Re = 10 (gray filled upward triangles), we have $l_c/d \lesssim 1$ due to the smooth, low curvature geometry of the interface. For Re = 60 (gray filled circles), l_c/d is larger

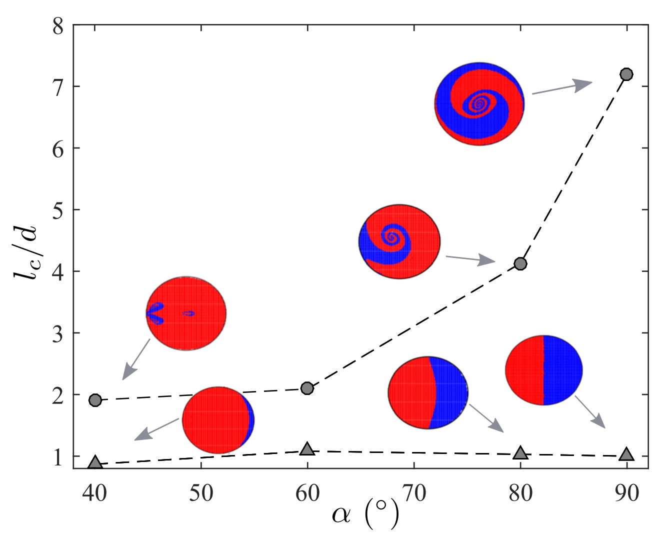

FIG. 12. Variation of the dimensionless length l_c/d of the interface separating the two fluids with the angle α for Re = 10 (gray filled upward triangles) and 60 (gray filled circles). Thumbnail pictures: distributions of the intersections of the flow lines of the two fluids for several values of α. Sections correspond to the outlet O_2.

than for $Re = 10$ due to the more complex interface geometry but remains of the order of 2 for $\alpha \lesssim 60°$. Instead, at higher angles, l_c/d increases sharply up to 7 for $\alpha \lesssim 90°$. This increase reflects the spiral geometry resulting from the large axial vorticity and will increase strongly the efficiency of mixing in practical cases. When molecular diffusion is present, the diffusion distance necessary to obtain a homogeneous mixing is of the order of the thickness of the arms of the spirals and is much smaller than when they are not present. The present choice of X-shaped junctions with two inlet channels facing each other (respectively, two outlet channels) favors the appearance, at high α and Re values, of axial vorticity (enhancing mixing) due to the location of the flow stagnation points away from the walls. For T-shaped junctions[22] and $Re \leq 150$, the symmetry of the flow is different and the stagnation points are located near the wall facing the outlet. Swirling takes then place as pairs of vortices, each one involving only one of the fluids, with a limited influence on mixing or related processes.

In the present work, axial vortices appear in the upper range of junction angles ($\alpha \gtrsim 65°$) and Reynolds numbers investigated ($Re \gtrsim 50$ in Fig. 8). The emergence of these vortices is detected from the variations of the axial vorticity $\langle \omega_{axial} \rangle$ averaged over the outlet volume V_{out}: this latter definition cancels the influence of the axial vorticity component due to the Poiseuille flow and makes $\langle \omega_{axial} \rangle$ very sensitive to the onset of axial vortex structures, as seen in Figs. 9(a) and 10(a). The critical number $Re_c(\alpha)$ of this instability is determined from the variation of $\langle \omega_{axial} \rangle$ with Re at a constant α: it decreases as α increases down to $Re_c = 50$ for $\alpha = 90°$. The increase in the axial vorticity with Re above the threshold is abrupt at this angle [Fig. 9(a)] and smoother at lower α's. The values of Re_c for the present X-shaped junctions are always lower than the corresponding ones in T-shaped junctions.

It is interesting to compare these results to those of Haward *et al.*[16] obtained in junctions of channels of rectangular cross sections with different aspect ratios and $\alpha = 90°$. These authors characterize the amplitude of this instability by the ratio ψ of the maximum along the axis (z) of the transverse velocity component v_y and the mean velocity V_m in the outlet (see Fig. 1). Their results are plotted as open symbols in Fig. 13. We have superimposed in the same graph data which we obtained in a similar way (see the figure caption) for $\alpha = 90°, 75°$, and $69°$. We note that in all cases, ψ is nonzero at $Re = Re_c$, implying that one deals with a subcritical instability, like for $d/w > 0.55$ in Ref. 16: this is a logical result, particularly for $\alpha = 90°$, if one approximates the tubes by rectangular channels with $d/w = 1$. As commonly done for subcritical instabilities, the points corresponding to $\epsilon < 0$ are obtained by letting first Re reach a value larger than Re_c, letting the instability develop, and, then, reducing Re to the desired value lower than Re_c.

For $\alpha = 90°$ and $75°$, the variations of ϵ with ψ are well fitted (continuous lines) in our experimental range by the polynomial variation found by Haward *et al.* Moreover, these variations are qualitatively similar to those obtained for $d/w = 1$ and 0.75 implying a similar type of instability in spite of the difference of the control parameters. For $\alpha = 69°$, the variation is only well fitted up to $\epsilon \sim 0.15$ and is then much slower. This variation is also very different from those obtained by Haward *et al.* for $d/w = 0.6$ and $d/w = 0.5$. This difference is likely due to the fact that in this range of angles, the vorticities $\langle \omega_{axial} \rangle$ and $\langle \omega_z \rangle$ become of the same order of magnitude.

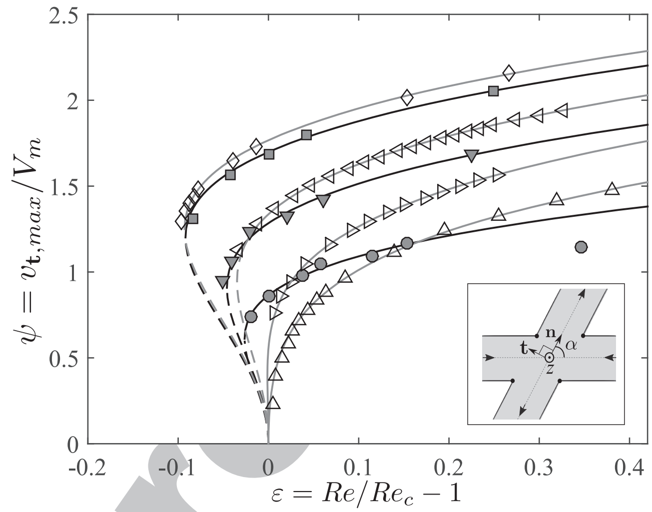

FIG. 13. Variations with the control parameter $Re/Re_c - 1$ of the order parameter $\psi = v_{\mathbf{t},max}/V_m$; Re_c = critical Reynolds number for the appearance of the axial vorticity, V_m = mean velocity in the outlet, $v_{\mathbf{t},max}$ = maximum value along the axis of the outlet axis of the transverse component of the velocity along the direction of the unit vector $\boldsymbol{t}$, perpendicular to $\boldsymbol{n}$, which points in the direction of the outlet channel. Dark gray symbols: results for angles $\alpha = 90°$ (gray filled squares), $75°$ (gray filled downward triangles), and $69°$ (gray filled circles). Open symbols: results of Haward *et al.*[16] for aspects ratios $d/w = 1$ (black empty diamonds), 0.75 (black empty left pointing triangles), 0.6 (black empty right pointing triangles), and 0.5 (black empty upward triangles) (d = channel height, w = width). Continuous lines: fits with Eq. (4) of Haward *et al.*[16] Inset: schematic view of the definition of the unit vectors in the junction.

The second important set of quantitative results provided by the simulations is the compared variations of the transverse vorticity $\langle \omega_z \rangle$ with α and Re in the 2D and 3D cases. As mentioned in Sec. I, an important issue is whether 2D simulations can represent a less expensive alternative to 3D ones in some ranges of values of α and Re.

For practical applications, unlike axial vortices, vortices of axis perpendicular to the plane of the junction do not enhance mixing but, instead, keep the flows of the two fluids separate because they bounce back directly into the nearest channel after entering the junction. If only one vortex is present like in Fig. 4(a), mixing only takes place if both fluids diffuse into the vortex and mix there: this will be quite slow but may be of practical interest in the case of reactive fluids requiring a rather long residence time to interact. Such exchange processes were previously studied for recirculations created by cellular instabilities.[23,24] When the junction angle is further reduced, additional vortices appear in the central region of the junction so that it is even more difficult to mix the incoming fluids. If, instead, the angle α is larger than a critical value $\alpha_c(Re)$, there are no vortices (see Figs. 7 and 8) and the two fluids flow side-by-side in the outlet channels: mixing may then be achieved through transverse molecular diffusion across the interface which remains a slow process but may be enhanced by axial vorticity (only in the 3D case) and/or time dependent flow components.

At low Reynolds numbers and angles α, the structure of 3D flows in junctions has been shown to be nearly bidimensional, as can be seen in Figs. 11(a), 11(c), and 11(e) for $\alpha = 15^\circ$ and $Re = 5$. However, the comparison of the 2D and 3D flow regime maps (Figs. 7 and 8) shows that even at these low Reynolds numbers, the number of transverse vortices corresponding to a given set of values of Re and α is generally lower in the 3D case than in the 2D one. Similarly, the critical angles of transition between different numbers of transverse vortices are significantly lower in 3D than in 2D. When the Reynolds number increases, the 3D flow fields differ still more from 2D ones due to the increasingly 3D structure of the streamlines, as seen, for $Re = 60$, in Figs. 5(a)–5(c) and Figs. 11(b), 11(d), and 11(f). Finally, the flow separation vortices appearing in the outlet channels downstream of the junction are much larger in the 2D case [Figs. 2(d) and 4(d)].

Regarding the quantitative variations of the vorticity components, $\langle \omega_z \rangle$ decreases steadily toward a low value in a similar way in the 2D and 3D cases as α increases from 15° to ~60°; this latter limit is close to the angle at which, in 3D, $\langle \omega_{axial} \rangle$ starts to increase from zero when an axial swirl appears. This suggests that the two phenomena might be related in the 3D case and might reflect a variation of the tilt angle of the vorticity with Re: further studies would be needed to test these hypotheses. Above $\alpha \sim 60^\circ$, $\langle \omega_z \rangle$ increases in both cases, but more weakly in 3D, and reaches a shallow maximum. On the other hand, the dependence of $\langle \omega_z \rangle$ on Re is remarkably different in the 2D and 3D simulations. While for 2D $\langle \omega_z \rangle$ increases always steadily with Re, its variation in the 3D geometry depends on α. At small angles for which $\langle \omega_{axial} \rangle = 0$ at all Re's investigated, the behaviors in the 2D and 3D cases are similar. Instead, for larger angles at which $\langle \omega_{axial} \rangle$ is not negligible, $\langle \omega_z \rangle$ retains a low value up to $Re \approx 50$ and increases sharply at higher Re's. Finally, $\langle \omega_z \rangle$ is negligible at $\alpha = 90^\circ$ for all Re's in both 2D and 3D simulations. This suggests an influence of the 3D nature of the flow on $\langle \omega_z \rangle$ even at moderate Reynolds numbers and an influence of the axial component of the vorticity when it appears.

Globally, the comparison of 2D and 3D simulations has shown that several features of the flow and of the vorticity $\langle \omega_z \rangle$ are qualitatively similar in the 2D and 3D simulations, particularly at low enough α and Re. However, many quantitative characteristics such as the variations of the transverse vorticity and the detailed map of existence of the different flow regimes differ significantly in the two types of simulations. These comparisons show therefore that while 2D simulations may provide simple models of physical transport mechanisms in junctions, they cannot make valid quantitative predictions even at low Reynolds numbers.

The present work uses junctions of circular channels relevant to many applications; it will be interesting to perform the same 3D simulations for junctions of channels with square or rectangular sections representative of some microfluidic circuits. In addition to these latter applications, this will allow one to determine whether a part of the difference between the variations of $\langle \omega_z \rangle$ in the 2D and 3D cases might be due to the use of a circular section (a rectangular or square one might give results more similar to the 2D ones). The Reynolds number has also been limited to low and moderate values ($Re \lesssim 90$) at which flows remain time independent, even though inertia plays an important part, as shown by the appearance of strongly tridimensional structures. It will be important, in future work, to determine the threshold for the onset of time dependent flows which, in particular, may enhance the interpenetration of the different fluids involved.[25,26]

ACKNOWLEDGMENTS

This work was supported by public grants overseen by the Comisión de Investigaciones Científicas de la Provincia de Buenos-Aires (CICPBA) through a "Proyecto de Fortalecimiento de Centros" (Reference No. FCCIC16) and by the French National Research Agency (ANR) through (i) ANR Bacflow No. AAPG 2015 and (ii) the "Laboratoire d'Excellence Physics Atom Light Mater" (LabEx PALM) as part of the "Investissements d'Avenir" program (No. ANR-10-LABX-0039). We also acknowledge support by the Consejo Nacional de Investigaciones Científicas y Técnicas (CONICET) and the Franco-Argentinian International Associated Laboratory in the Physics and Mechanics of Fluids (LIA PMF-FMF).

REFERENCES

[1] H. Stone, A. Stroock, and A. Ajdari, "Engineering flows in small devices: Microfluidics toward a lab-on-a-chip," Annu. Rev. Fluid Mech. **36**, 381 (2004).
[2] G. Cai, L. Xue, H. Zhang, and J. Lin, "A review on micromixers," Micromachines **8**, 274 (2017).
[3] C.-X. Zhao, L. He, S. Z. Qiao, and A. P. Middelberg, "Nanoparticle synthesis in microreactors," Chem. Eng. Sci. **66**, 1463 (2011).
[4] K. C. Bhargava, B. Thompson, and N. Malmstadt, "Discrete elements for 3D microfluidics," Proc. Natl. Acad. Sci. U. S. A. **111**, 15013 (2014).
[5] N.-T. Nguyen and Z. Wu, "Micromixers—A review," J. Micromech. Microeng. **15**, R1 (2005).
[6] S. Thomas, T. Ameel, and J. Guilkey, "Mixing kinematics of moderate Reynolds number flows in a T-channel," Phys. Fluids **22**, 013601 (2010).
[7] S. H. Wong, M. C. Ward, and C. W. Wharton, "Micro T-mixer as a rapid mixing micromixer," Sens. Actuators, B **100**, 359 (2004).
[8] D. Bothe, C. Stemich, and H.-J. Warnecke, "Fluid mixing in a T-shaped micro-mixer," Chem. Eng. Sci. **61**, 2950 (2006).
[9] I. Lashgari, O. Tammisola, V. Citro, M. P. Juniper, and L. Brandt, "The planar X-junction flow: Stability analysis and control," J. Fluid Mech. **753**, 1 (2014).
[10] T. Perkins, D. Smith, and S. Chu, "Single polymer dynamics in an elongational flow," Science **276**, 2016 (1997).
[11] K.-W. Hsiao, C. Sasmal, J. Ravi Prakash, and C. M. Schroeder, "Direct observation of DNA dynamics in semi-dilute solutions in extensional flow," J. Rheol. **61**, 151 (2017).
[12] P. E. Arratia, C. C. Thomas, J. Diorio, and J. P. Gollub, "Elastic instabilities of polymer solutions in cross-channel flow," Phys. Rev. Lett. **96**, 144502 (2006).
[13] R. J. Poole, M. A. Alves, and P. J. Oliveira, "Purely elastic flow asymmetries," Phys. Rev. Lett. **99**, 164503 (2007).
[14] D. Lee, Y.-T. Chen, and T.-Y. Bai, "A study of flows in tangentially crossing micro-channels," Microfluid. Nanofluid. **7**, 169 (2009).
[15] M. Cachile, L. Talon, J. M. Gomba, J. P. Hulin, and H. Auradou, "Stokes flow paths separation and recirculation cells in X-junctions of varying angle," Phys. Fluids **24**, 021704 (2012).
[16] S. J. Haward, R. J. Poole, M. A. Alves, P. J. Oliveira, N. Goldenfeld, and A. Q. Shen, "Tricritical spiral vortex instability in cross-slot flow," Phys. Rev. E **93**, 031101 (2016).
[17] Y. Saad and M. Schultz, "GMRES: A generalized minimal residual algorithm for solving nonsymmetric linear systems," SIAM J. Sci. Stat. Comput. **7**, 856 (1986).
[18] S. Mittal, "Computation of three-dimensional flows past circular cylinder of low aspect ratio," Phys. Fluids **13**, 177 (2001).
[19] A. Noorani, R. Vinuesa, L. Brandt, and P. Schlatter, "Aspect ratio effect on particle transport in turbulent duct flows," Phys. Fluids **28**, 115103 (2016).

[20]A. C. Hindmarsh, P. N. Brown, K. E. Grant, S. L. Lee, R. Serban, D. E. Shumaker, and C. S. Woodward, "Sundials: Suite of nonlinear and differential/algebraic equation solvers," ACM Trans. Math. Software **31**, 363 (2005).
[21]P. G. Correa, "Characterization of flows in millimetric junctions," M.Sc. thesis, UNCPBA, March 2016, http://www.ridaa.unicen.edu.ar/xmlui/handle/123456789/568.
[22]N. Kockmann, T. Kiefer, M. Engler, and P. Woias, "Convective mixing and chemical reactions in microchannels with high flow rates," Sens. Actuators, B **117**, 495 (2006).
[23]B. I. Shraiman, "Diffusive transport in a Rayleigh-Bénard convection cell," Phys. Rev. A **36**, 261 (1987).
[24]E. Guyon, Y. Pomeau, J. P. Hulin, and C. Baudet, "Dispersion in the presence of recirculation zones," Nucl. Phys. B, Proc. Suppl. **2**, 271 (1987).
[25]W. Mao and J. Xu, "Micromixing enhanced by pulsating flows," Int. J. Heat Mass Transfer **52**, 5258 (2009).
[26]A. Dodge, A. Hountondji, M. C. Jullien, and P. Tabeling, "Spatiotemporal resonances in a microfluidic system," Phys. Rev. E **72**, 056312 (2005).